

Modeling of MHD waves in the solar corona

Pieter Luyten, Tomas Reunbrouck

May 2, 2020

Contents

1	Introduction	3
2	Theoretical background	4
2.1	Hydrodynamic theory	4
2.1.1	Fluid equations	4
2.1.2	Hydrodynamic linear waves	5
2.1.3	Hydrodynamic shocks	6
2.2	Magnetohydrodynamic theory	8
2.2.1	What exactly is a plasma?	8
2.2.2	Magnetohydrodynamic fluid equations	8
2.2.3	Magnetohydrodynamic waves	11
2.2.4	Magnetohydrodynamic shocks	13
2.2.5	Group speed	13
2.3	Units	14
3	Modeling shock waves	16
3.1	Hydrodynamic shock wave	16
3.2	Magnetohydrodynamic shock wave	19
4	Coronal hole	22
4.1	Initial and boundary conditions	22
4.2	Terminology	24
4.3	Results coronal hole	25
4.4	Results coronal plume	26
5	Summary	28
6	Final Remarks	28

1 Introduction

The lay of the land

This report discusses simulation results of the plasma in the solar corona in accordance with the theory of magnetohydrodynamics (MHD). We aim give an qualitative interpretation of our simulation data based on the MHD equations for an ideal plasma.

Studying the behaviour of a plasma based on analytically acquired solutions of the MHD equations is very complicated. Thus, it is useful to attain some solutions numerically and interpret the results by means of visualizations.

In this manner we have completed an analysis of the behaviours of an idealised plasma for different boundary conditions. For each case we have investigated the influence of changes in the initial conditions by running the simulation in parallel for different values of the initial variables and comparing the outputs.

Goal of this report

As mentioned, the main purpose of the project was to gain a basic understanding of the nature of the plasma in the solar corona. Specifically MHD waves are of great interest as they are directly observable in satellite observations of the sun. Therefore, we shall focus our report on them. Concretely, we discuss two compelling examples of MHD waves: the MHD blastwave and the interaction of an MHD wave with a coronal hole.

For the first problem we have simulated an MHD blastwave under the influence of a very powerful magnetic field. Visualizations of the output data have shown that the results are quite distinct for different values of the magnetic field's strength. We have also simulated a blastwave under normal hydrodynamic (HD) conditions. This HD blastwave provides the case where the field strength is 0.

Secondly, we discuss a simulation where we had an MHD wave run into a coronal hole. This hole is part of the boundary conditions for this problem. It consists of a sharp drop in pressure and density. As one would expect, its effect on the wave is quite striking and we shall discuss it in detail.

The software used

The software that was used for the numerical solutions is called PLUTO. This is an open source code written specifically for the purpose of plasma simulations.

Taken from the paper first introducing the PLUTO code, Mignone et al. (2007): "*The code is particularly suitable for time-dependent, explicit computations of highly supersonic flows in the presence of strong discontinuities, and it can be employed under different regimes, i.e., classical, relativistic unmagnetized, and magnetized flows*"

PLUTO implements some high-resolution shock-capturing (HSRC) schemes to solve the hydrodynamic and magnetohydrodynamic equations, either in Galilean or relativistic form, in 1, 2 or 3 dimensions Mignone et al. (2007). PLUTO was developed by the Department of Physics at Torino University. Mignone and et al. (2018)

2 Theoretical background

2.1 Hydrodynamic theory

While the main focus of this project is the numerical modeling of waves in the solar corona, some theoretical background is important to frame the results of our simulations. Furthermore, this knowledge gives some insight in the assumptions that are made in deriving the magnetohydrodynamic equations and when they are valid.

We shall begin by a discussion of the cleaner and more transparent theory of ideal hydrodynamics before delving into the much more complicated and cluttered realm of magnetohydrodynamic theory. However, we emphasize that there is no fine line between the two and that indeed, HD theory can be seen as the special case of MHD theory in with a negligible magnetic field.

2.1.1 Fluid equations

The theory in this section is adapted from Doorsselaere (2019). For the first task a non-viscous Newtonian fluid is considered. Heat conduction and dissipation is neglected as well. This type of fluid obeys the Euler equations for conservation of mass, momentum and internal energy:

$$\begin{aligned} \frac{d\rho}{dt} + \rho \nabla \cdot \mathbf{v} &= 0 \\ \rho \frac{d\mathbf{v}}{dt} &= -\nabla p + \mathbf{F} \\ \frac{dp}{dt} - \frac{\gamma p}{\rho} \frac{d\rho}{dt} &= 0 \end{aligned} \quad (1)$$

These are the Euler equations in Lagrangian form, with time derivatives following the fluid, hence the total derivatives with respect to time. PLUTO does the fluid simulation using a static grid. Therefore we need the equations in their Eulerian form: partial derivatives with respect to time instead of total derivatives. This change of derivatives can be carried out using the following relation, found in Doorsselaere (2019), section 2.4:

$$\frac{df}{dt} = \frac{\partial f}{\partial t} + (\mathbf{v} \cdot \nabla) f \quad (2)$$

where $f(x, y, z, t)$ is a function that describes a property of the fluid. The resulting equations could also have been re-derived using an Eulerian view to begin with. In any case the result is the same:

$$\begin{aligned} \frac{\partial \rho}{\partial t} + \nabla \cdot (\rho \mathbf{v}) &= 0 \\ \frac{\partial}{\partial t} (\rho \mathbf{v}) &= \nabla \cdot (-p \mathbb{I} - \rho \mathbf{v} \mathbf{v}) + \mathbf{F} \\ \frac{\partial}{\partial t} \left(\rho \left(\frac{v^2}{2} + \mathcal{U} \right) \right) &= \mathbf{F} \cdot \mathbf{v} - \nabla \cdot \left(\rho \left(\frac{v^2}{2} + \mathcal{U} \right) \mathbf{v} + p \mathbf{v} \right) \end{aligned} \quad (3)$$

Next introduced is the variable $\mathbf{m} = \rho \mathbf{v}$, the momentum density. The energy density \mathcal{U} can be split in the thermal energy ρe and gravitational potential energy $\rho \Phi$. Let $E_t = e\rho + \frac{v^2}{2}$. The only external force is $\mathbf{F} = \rho \mathbf{g}$. Carrying out these substitutions leads to the equations in section 6 in the PLUTO manual Mignone and et al. (2018):

$$\begin{aligned}
\frac{\partial \rho}{\partial t} + \nabla \cdot \mathbf{m} &= 0 \\
\frac{\partial \mathbf{m}}{\partial t} + \nabla \cdot (\mathbf{m}\mathbf{v} + p\mathbb{I}) &= -\rho \nabla \Phi + \rho \mathbf{g} \\
\frac{\partial}{\partial t} (E_t + \rho \Phi) + \nabla \cdot ((E_t + p + \rho \Phi) \mathbf{v}) &= \mathbf{m} \cdot \mathbf{g}
\end{aligned} \tag{4}$$

These equations are soluble given an appropriate equation of state, expressing the thermal energy density ρe as a function of p and ρ . For the purpose of finding such an equation, assume the gas to be calorically ideal. That is, presuppose a constant number of degrees of freedom f for its constituent molecules. From this we extract the adiabatic constant:

$$\gamma = \frac{f+2}{f} \tag{5}$$

This expression which can be rewritten as

$$f = \frac{2}{\gamma - 1}$$

Finally, the necessary equation of state is found Doorselaere (2019)[Subsection 3.6.5] :

$$\rho e = \frac{f}{2} n k_B T = \frac{p}{\gamma - 1}$$

2.1.2 Hydrodynamic linear waves

We start again from the ideal fluid equations as given in eq. (3) and linearize them. For this we rewrite the quantities ρ and p as a background density ρ_0 and pressure p_0 with slight deviations ρ_1 , p_1 . Furthermore, assume that there are no external forces acting on the fluid. The linearised equations are:

$$\begin{aligned}
\frac{\partial \rho_1}{\partial t} + \rho_0 \nabla \cdot \mathbf{v} &= 0 \\
\rho_0 \frac{\partial \mathbf{v}}{\partial t} &= -\nabla p_1 \\
\frac{\partial p_1}{\partial t} &= \frac{\gamma p_0}{\rho_0} \frac{\partial \rho_1}{\partial t}
\end{aligned} \tag{6}$$

By acting with ∇ on the second equation and using the first to substitute $\rho_0 \nabla \cdot \mathbf{v}$ we find the following relation:

$$\frac{\partial^2 \rho_1}{\partial t^2} = -\nabla^2 p_1$$

Acting with $\frac{\partial}{\partial t}$ on the last equation and substituting the previous expression yields

$$\frac{\partial^2 p_1}{\partial t^2} + \frac{\gamma p_0}{\rho_0} \nabla^2 p_1 = 0$$

which is the wave equation with wave speed

$$v_s = \sqrt{\frac{\gamma p_0}{\rho_0}} \tag{7}$$

the speed of sound in the ideal fluid, and the phase- and group speed of linear sound waves. Similar expressions are found for the other variables. This wave speed can be found by substituting a plane

wave of the form $p_1 = A \exp(i(\omega t - \mathbf{k} \cdot \mathbf{x}))$. Substituting this expression in the wave equation for p_1 leads to the dispersion relation:

$$\omega^2 = k^2 v_s^2. \quad (8)$$

The group velocity is given by

$$\mathbf{v}_g = \frac{\partial \omega}{\partial \mathbf{k}} = v_s \hat{\mathbf{k}} \quad (9)$$

from which we conclude that these waves are non-dispersive Doorselaere (2019)[Chapter 6].

2.1.3 Hydrodynamic shocks

Now we shall reconsider one of the least convincing assumptions made for the derivations of the fluid equations: that of perfectly continuous background variables. In reality, we might encounter very sudden changes in the scalar variable density ρ and vectorial variable velocity \mathbf{v} . To have the theory of ideal fluids take this into account, we can introduce these jumps in the variables as mathematical discontinuities. Such a discontinuity is appropriately called a ‘shock’. We are interested in how these shocks move through the fluid. The derivation of their motion is quite straightforward.

Start from the continuity equation in its Eulerian form in 1D

$$\frac{\partial \rho}{\partial t} + \frac{\partial(\rho v)}{\partial x} = 0 \quad (10)$$

Of course, this equation assumes that ρ and ρv are continuous variables with continuous partial derivatives. Rewrite the equation so that over a distance Δx and a duration Δt the variables ρ and ρv experience a change $\Delta \rho$ and $\Delta \rho v$. This gives the much less elegant version

$$\frac{\Delta \rho}{\Delta t} + \frac{\Delta(\rho v)}{\Delta x} = 0 .$$

If this were the perfectly continuous case we would now let $\Delta x, \Delta t \rightarrow 0$, resulting in eq. (10). However, we might also say that the transition is not smooth and that for $\Delta x, \Delta t \rightarrow 0$ the jump remains: $\Delta \rho, \Delta \rho v \rightarrow \Delta \rho, \Delta \rho v$. Rewrite the equations to see what this means:

$$\frac{\Delta x}{\Delta t} \Delta \rho + \Delta(\rho v) = 0 .$$

Then for $\Delta x, \Delta t \rightarrow 0$ we get

$$\frac{\partial x}{\partial t} \Delta \rho + \Delta(\rho v) = -V_S \Delta \rho + \Delta(\rho v) = 0 \quad (11)$$

where V_S is the shock speed. This relation is the first hydrodynamic shock condition. To generalize it beyond 1D, it suffices to take $\mathbf{v} \cdot \mathbf{n}$ instead of v where \mathbf{n} is the unit normal vector on the shock wave front pointing towards the region with lower pressure. It looks as follows:

$$-V_S \Delta(\rho v) + \Delta(\rho \mathbf{v} \cdot \mathbf{n}) = 0 . \quad (12)$$

The minus sign in front of V_S is merely a matter of orientation. In eq. (11) the orientation is along the positive x-axis. In eq. (12) it is along the unit vector \mathbf{n} . This is the first of the three HD *Rankine–Hugoniot* relations. The other two can analogously be derived from the Eulerian form of the momentum and energy equations in eq. (3). The three Rankine–Hugoniot conditions are

$$\begin{aligned}
V_S \Delta \rho &= \mathbf{n} \cdot \Delta(\rho \mathbf{v}) \\
V_S \Delta(\rho \mathbf{v}) &= \mathbf{n} \cdot \Delta(\rho \mathbf{v} \mathbf{v} + p \mathbb{I}) \\
V_S \Delta E_t &= \mathbf{n} \cdot \Delta\left(\rho \left(e + \frac{v^2}{2} + \frac{p}{\rho}\right) \mathbf{v}\right)
\end{aligned} \tag{13}$$

Now, for the purposes of this report we would like to write a shock condition in terms of the shock speed as a function of the initial conditions p_0, ρ_0, v_0 and the final pressure p_1 since pressure is the variable on which we shall be focusing in the simulation data results. Consider a pressure discontinuity $\Delta p = p_1 - p_0$. Use the 1D mass and momentum equations to obtain that

$$V_S^2 = \frac{\Delta \rho v^2 + p}{\Delta \rho} \tag{14}$$

Assume that $v_0 = 0$. This assumption may not seem entirely reasonable, but is very helpful in simplifying the problem and will be correct for most of our purposes. Furthermore, we shall see that it can be easily removed when we wish. Combining eq. (14) with the third shock condition derived from the energy equation, this then results in

$$V_S^2 = v_s^2 + \frac{\gamma + 1}{2\rho_0} \Delta p \tag{15}$$

where $v_s = \sqrt{\frac{\gamma p_0}{\rho_0}}$ is the speed of sound under the initial conditions. Notice that for $\Delta p = 0$ this expression gives $V_S = v_s$ as we should expect Goedbloed and Poedts (2004)[Subsection 4.5.1].

In case we cannot assume $v_0 = 0$ (and do not wish to view the problem from a moving reference frame) the expression changes only slightly.

$$\begin{aligned}
(V_S - v_0)^2 &= v_s^2 + \frac{\gamma + 1}{2\rho_0} \Delta p \\
V_S &= v_0 + \sqrt{v_s^2 + \frac{\gamma + 1}{2\rho_0} \Delta p}
\end{aligned} \tag{16}$$

Of course, for the 3D case, one simply writes

$$V_S = \mathbf{n} \cdot \mathbf{v}_0 + \sqrt{v_s^2 + \frac{\gamma + 1}{2\rho_0} \Delta p} \tag{17}$$

2.2 Magnetohydrodynamic theory

2.2.1 What exactly is a plasma?

A brief justification of some basic assumptions is in place. As mentioned, we presuppose that the solar corona consists of an ideal plasma. That is, a highly ionised gas with smooth background conditions. A gas of this type should demonstrate a ‘collective behaviour’ which is necessary for the ideal MHD equations to be sufficiently accurate. By ‘collective behaviour’, we mean the following.

A plasma consists of positively charged ions and negatively charged electrons. To be able to assume the ideal MHD theory we must have that the kinetic energy of these particles sufficiently outweighs the potential energy produced by the pairwise Coulomb interactions. In other words, we require $\frac{KE}{PE} \gg 1$. If this is indeed the case we may presume that we are working with a collection of particles that interact on a smooth background.

Such a smooth background is achieved by a phenomenon called ‘electric screening’. This is the effect by which positively charged ions are electrically screened from each other - in that their mutual Coulomb interaction becomes negligible - by a surrounding cloud of electrons.

Consider any such ion. We can write its circumambient electric potential in a system of mobile charged particles as

$$\phi \sim \frac{1}{r} e^{-rk_D}$$

where $k_D = \frac{1}{\lambda_D}$ and λ_D is the Debye length. The reason why the Debye length is important for our purposes is that it traces the boundary of where the motion of the particles begins to outweigh the electric potential. We can see this because for a given electric charge Q

$$\frac{KE}{PE} \sim \frac{T}{\frac{Q}{\lambda_D}} \sim \frac{\lambda_{MFP}}{\lambda_D}$$

where λ_{MFP} is the mean length of a free particle path. This clarifies the significance of the strong inequality $\frac{KE}{PE} \gg 1$: the charged particles move quasi freely through the plasma with very infrequent occurrence of one to one electromagnetic interaction.

Since the temperature in the solar corona is of the order of $10^6 K$ we may assume that these ratios are sufficiently large to consider the ion gas as a collection of charged particles which behave collectively, which is what constitutes a plasma. Goedbloed and Poedts (2004)

2.2.2 Magnetohydrodynamic fluid equations

Since the aim of this project is mainly using simulation software to acquire an understanding of the behaviour of waves in a plasma and the subject of magnetohydrodynamic theory is particularly complicated, we will merely state the relevant results as theoretical background for our simulation results and only briefly discuss the derivations, without delving into every technical detail. That being said, some theory is required to properly appreciate the interpretation and significance of the simulation results.

There are two common approaches in the literature for deriving the MHD equations. They are either derived from kinetic gas theory, or postulated with added justification as to why they provide an accurate description of plasma physics.

We will now sketch the first approach in order to get some insight into the underlying assumptions of the theory. A plasma is an ionised gas consisting of positively and negatively charged particles.

In the case of the solar corona, the plasma mainly consists of ionised hydrogen. Therefore the negatively charged particles are free electrons whereas the positively charged particles are protons, which are much heavier than electrons. When the characteristic time scales τ_e and τ_i between two collisions of electrons, respectively ions, is much smaller than characteristic time scales τ_f at which the macroscopic variables change, we can use a fluid description. At these timescales the mutual interactions of individual particles are no longer relevant Goedbloed and Poedts (2004)[Subsection 1.4.1, 1.4.2].

The plasma can then be described as two different fluids, commonly referred to as the *two-fluid theory* where the electron gas is one fluid and the proton gas the other. The next assumption that is made, is that the relaxation time τ_T until the electron fluid and ion fluid reach thermal equilibrium following a slight disturbance, is also a lot smaller than τ_f . Finally, we assume that the fluid has no net charge. Not globally, but also not locally. This means that in every large enough volume, for every ion with charge Q , there is approximately a charge $-Q$ due to electrons in this volume. When all this applies, the variables describing the different fluids can be averaged over or added together, to describe the plasma as a single fluid Goedbloed and Poedts (2004)[Subsection 2.4.1].

The MHD equations can then be found by adding the Maxwell equations to the HD equations. However, there is one complication: the HD equations are invariant under Galilean transformations, whereas the Maxwell equations are invariant under Lorentz transformations. Thus we cannot simply combine them with the HD equations and expect a consistent picture. In order to solve this, the term for the displacement current $\epsilon_0 \frac{\partial \mathbf{E}}{\partial t}$ is removed, Ogilvie (2016) [chapter 3], Goedbloed and Poedts (2004)[Subsection 2.4.1, 3.3.1, 3.4.2] which results in a set of equations that are invariant under Galilean transformations.

Understanding the averaging process, which brings us from the two-fluid theory to the description given by the MHD equations, is important for understanding what the plasma variables actually represent and whether this representation is an accurate depiction of the state of the plasma.

Denote with n_α the number density of a certain type of particle α , with m_α the mass of one such particle, with \mathbf{u}_α the velocity of a fluid element, and with p_α the pressure. Let the subscript e denote variables concerning the electron gas and i variables describing the ion gas. The variables describing the plasma are the following linear combinations of variables describing the electron and ion gasses:

$$\begin{aligned} \rho &= n_e m_e + n_i m_i \\ \mathbf{v} &= (n_e m_e \mathbf{u}_e + n_i m_i \mathbf{u}_i) / \rho \\ \mathbf{J} &= -e(n_e \mathbf{u}_e - Z n_i \mathbf{u}_i) \\ p &= p_e + p_i \end{aligned} \quad (18)$$

Where e is the charge of an electron and Z the charge number of an ion representing its charge as a whole multiple of the electron charge. The first equation is the *total mass density*, the second is the *center of mass velocity*, the third the *current density*, and the last one describes the *total pressure*.

Finally, the viscosity and heat flow are neglected as in the ordinary HD case. Furthermore, for the ideal MHD case the resistivity of the fluid is ignored as well. The extra equations we need are then:

$$\begin{aligned} \frac{\partial \mathbf{B}}{\partial t} &= -\nabla \times \mathbf{E} \\ \nabla \cdot \mathbf{B} &= 0 \\ \nabla \times \mathbf{B} &= \mu_0 \mathbf{J} \end{aligned}$$

We do not need an equation relating the charge distribution to the electric field in the first equation since we assumed the fluid is locally neutral. Moreover, the displacement term in the third equation has been neglected, see Ogilvie (2016) [chapter 3].

Adding everything together such as in Goedbloed and Poedts (2004)[Subsection 4.1.1] yields the ideal MHD equations:

$$\begin{aligned}
& \frac{\partial \rho}{\partial t} + \nabla \cdot (\rho \mathbf{v}) = 0 \\
& \rho \left(\frac{\partial \mathbf{v}}{\partial t} + \mathbf{v} \cdot \nabla \mathbf{v} \right) + \nabla p - \mathbf{J} \times \mathbf{B} = 0 \\
& \frac{\partial p}{\partial t} + \mathbf{v} \cdot \nabla p + \gamma p \nabla \cdot \mathbf{v} = 0 \\
& \frac{\partial \mathbf{B}}{\partial t} - \nabla \times (\mathbf{v} \times \mathbf{B}) = 0
\end{aligned} \tag{19}$$

Here

$$\mathbf{J} = \frac{\nabla \times \mathbf{B}}{\mu_0}.$$

We need one additional equation which the initial condition has to satisfy:

$$\nabla \cdot \mathbf{B} = 0$$

This excludes magnetic monopoles from the description. By acting with $\nabla \cdot$ on the fourth equation in eq. (19) we see that if the initial equation satisfies $\nabla \cdot \mathbf{B} = 0$, the condition is automatically satisfied for all later times:

$$\frac{\partial(\nabla \cdot \mathbf{B})}{\partial t} = 0$$

The equations used by PLUTO in the ideal MHD case have a slightly different form Mignone and et al. (2018) :

$$\begin{aligned}
& \frac{\partial \rho}{\partial t} + \nabla \cdot (\mathbf{m}) = 0 \\
& \frac{\partial \mathbf{m}}{\partial t} + \nabla \cdot \left[\mathbf{m} \mathbf{v} - \mathbf{B} \mathbf{B} + I \left(p + \frac{B^2}{2} \right) \right]^T = -\rho \nabla \Phi + \rho \mathbf{g} \\
& \frac{\partial \mathbf{B}}{\partial t} + \nabla \times (c \mathbf{E}) = 0 \\
& \frac{\partial(E_t + \rho \Phi)}{\partial t} + \nabla \cdot [(E_t + p_t + \rho \Phi) \mathbf{v} - \mathbf{B}(\mathbf{v} \cdot \mathbf{B})] = \mathbf{m} \cdot \mathbf{g}
\end{aligned} \tag{20}$$

where, as with the HD equations, $\mathbf{m} = \rho \mathbf{v}$ and E_t is the total energy density, this time with an extra term for the magnetic field:

$$E_t = \rho e + \frac{\rho v^2 + B^2}{2}$$

$c \mathbf{E}$ is given by:

$$c \mathbf{E} = -\mathbf{v} \times \mathbf{B}$$

Note that the equations do not formally depend on the speed of light, but it is kept in the equations for consistency with the relativistic case Goedbloed and Poedts (2004) [Subsection 4.1.1].

Lastly we introduce the plasma- β . This is the ratio of the mechanical pressure p and the magnetic pressure $\frac{B^2}{2\mu_0}$:

$$\beta = \frac{p}{B^2/2\mu_0}$$

When β is small, the magnetic effects dominate the classic hydrodynamic effects and when β is large we approximate the hydrodynamic situation. This parameter will be frequently used to choose simulation parameters, as well as in the analysis of the simulation results.

2.2.3 Magnetohydrodynamic waves

The following discussion is largely based on Fitzpatrick (n.d.) [Magnetohydrodynamic Fluids] and Goedbloed and Poedts (2004) recompile. For the discussion concerning linear magnetohydrodynamic waves, we take as the initial condition with a homogeneous plasma in equilibrium. Denote with ρ_0 , p_0 , \mathbf{v}_0 and \mathbf{B}_0 these equilibrium values. To derive the equations for the waves, consider slight perturbations ρ_1 , p_1 , \mathbf{v}_1 and \mathbf{B}_1 of this equilibrium state, just like what was done to find the HD waves.

Firstly, rewrite the basic MHD equations into a form which is easier to linearise, this means that we shall remove the cross products in the original equations as follows:

$$\begin{aligned} -\mathbf{J} \times \mathbf{B} &= -(\nabla \times \mathbf{B}) \times \mathbf{B} = (\nabla \mathbf{B}) \cdot \mathbf{B} - \mathbf{B} \cdot \nabla \mathbf{B} \\ \nabla \times \mathbf{E} &= -\nabla \times (\mathbf{v} \times \mathbf{B}) = \mathbf{B} \nabla \cdot \mathbf{v} + \mathbf{v} \cdot \nabla \mathbf{B} - \mathbf{B} \cdot \nabla \mathbf{v} \end{aligned} \quad (21)$$

The MHD equations now become

$$\begin{aligned} \frac{\partial \rho}{\partial t} + \nabla \cdot (\rho \mathbf{v}) &= 0 \\ \rho \frac{\partial \mathbf{v}}{\partial t} + \rho \mathbf{v} \cdot \nabla \mathbf{v} + (\gamma - 1) \nabla(\rho e) + (\nabla \mathbf{B}) \cdot \mathbf{B} - \mathbf{B} \cdot \nabla \mathbf{B} &= 0 \\ \frac{\partial e}{\partial t} + \mathbf{v} \cdot \nabla e + (\gamma - 1) e \nabla \cdot \mathbf{v} &= 0 \\ \frac{\partial \mathbf{B}}{\partial t} + \mathbf{v} \cdot \nabla \mathbf{B} + \mathbf{B} \nabla \cdot \mathbf{v} - \mathbf{B} \cdot \nabla \mathbf{v} &= 0 \end{aligned} \quad (22)$$

Of course the requirement that $\nabla \cdot \mathbf{B} = 0$ remains. In this form the equations can easily be linearised:

$$\begin{aligned} \frac{\partial \rho_1}{\partial t} + \nabla \cdot (\rho_0 \mathbf{v}_1) &= 0 \\ \rho_0 \frac{\partial \mathbf{v}_1}{\partial t} + (\gamma - 1) \nabla(\rho_1 e_0) + \nabla(\rho_0 e_1) + (\nabla \mathbf{B}_1) \cdot \mathbf{B}_0 - \mathbf{B}_0 \cdot \nabla \mathbf{B}_1 &= 0 \\ \frac{\partial e_1}{\partial t} + (\gamma - 1) e_0 \nabla \cdot \mathbf{v}_1 &= 0 \\ \frac{\partial \mathbf{B}_1}{\partial t} + \mathbf{B}_0 \nabla \cdot \mathbf{v}_1 - \mathbf{B}_0 \cdot \nabla \mathbf{v}_1 &= 0 \end{aligned} \quad (23)$$

The second one of eq. (23) is the linearised momentum equation. We shall work from this one as it lends itself the most for our discussion of ideal MHD waves, because it directly describes flow velocity. Plugging the other three into this equation gives us the essential equation for ideal MHD waves:

$$\frac{\partial^2 \mathbf{v}_1}{\partial t^2} = \left((\mathbf{v}_a \nabla)^2 \mathbb{I} + (v_a^2 + v_s^2) \nabla \nabla - \mathbf{v}_a \cdot \nabla (\nabla \mathbf{v}_a + \mathbf{v}_a \nabla) \right) \cdot \mathbf{v}_1 \quad (24)$$

where

$$v_s = \sqrt{\frac{\gamma p_0}{\rho_0}} \quad (25)$$

and

$$\mathbf{v}_a = \frac{\mathbf{B}_0}{\sqrt{\rho_0}}. \quad (26)$$

We introduce the constants v_s and \mathbf{v}_a as they will be the wave velocities of the solutions of wave equation eq. (24). The constant v_s is the acoustic speed known from ordinary hydrodynamics. The constant \mathbf{v}_a is known as the *Alfvén* velocity and it is a vector in the same direction as the background magnetic field \mathbf{B}_0 .

Notice that if we set $\mathbf{B} = 0$ eq. (24) becomes

$$\frac{\partial^2 \mathbf{v}_1}{\partial t^2} = v_s^2 \nabla^2 \mathbf{v}_1$$

which is exactly what we would expect as this is wave equation in the regular hydrodynamic case. This is an important sanity check for our method.

Next we seek sinusoidal wave solutions. For now we shall also limit the discussion to waves in the velocity vector field as the waves in the scalar pressure and density fields and the magnetic vector field can easily be expressed in terms of the velocity field using eq. (23). The solutions we search are of the form

$$\mathbf{v}_1 = \bar{\mathbf{v}} \exp(i(\omega t - \mathbf{k} \cdot \mathbf{x})) .$$

Under the constraint of having to provide sinusoidal wave solutions eq. (24) becomes

$$[(\omega^2 - (\mathbf{k} \cdot \mathbf{b})^2) \mathbb{I} - (b^2 + c^2) \mathbf{k} \mathbf{k} + \mathbf{k} \cdot \mathbf{b} (\mathbf{k} \mathbf{b} + \mathbf{b} \mathbf{k})] \cdot \bar{\mathbf{v}} = 0 . \quad (27)$$

Without any loss of generality we may assume that $\mathbf{v}_a = (v_a, 0, 0)$ and $\mathbf{k} = (k_x, k_y, 0) = (k \cos \theta, k \sin \theta, 0)$ where θ is the angle between \mathbf{v}_a and \mathbf{k} . Filling in these into eq. (27) results in

$$\begin{pmatrix} \omega^2 - k_x^2 v_s^2 & -k_y k_x v_s^2 & 0 \\ -k_y k_x v_s^2 & \omega^2 - k_y^2 (v_a^2 + v_s^2) - k_x^2 v_a^2 & 0 \\ 0 & 0 & \omega^2 - k_x^2 v_a^2 \end{pmatrix} \begin{pmatrix} \bar{v}_x \\ \bar{v}_y \\ \bar{v}_z \end{pmatrix} = \begin{pmatrix} 0 \\ 0 \\ 0 \end{pmatrix} \quad (28)$$

This has a non-trivial solutions when the determinant of the matrix in eq. (28) is equal to 0. This results in the dispersion relation

$$(\omega^2 - k^2 v_a^2 \cos^2 \theta) (\omega^4 - \omega^2 k^2 (v_a^2 + v_s^2) + v_a^2 v_s^2 k^4 \cos^2 \theta) = 0 . \quad (29)$$

We shall first discuss the factor $(\omega^4 - \omega^2 k^2 (v_a^2 + v_s^2) + v_a^2 v_s^2 k^4 \cos^2 \theta)$ of which the roots are

$$\omega_{\pm}^2 = \frac{k^2}{2} \left[v_a^2 + v_s^2 \pm \sqrt{(v_a^2 + v_s^2)^2 - 4v_a^2 v_s^2 \cos^2 \theta} \right] \quad (30)$$

These solutions correspond to the so-called fast (+) and slow (-) magnetosonic waves. Notice that because $(v_a^2 + v_s^2)^2 - 4v_a^2 v_s^2 \cos^2 \theta \geq (v_a^2 - v_s^2)^2 \geq 0$ the square root can always be taken. One can readily see that they are the result of a quite complicated interplay between the hydrodynamic and magnetic sides of the story. We shall rely on the simulations to get a better understanding of their behaviour.

The only root of the first factor in eq. (29) is $\omega^2 = k^2 v_a^2 \cos^2 \theta$. This solution is of great interest as it does not contain the same complicated magnetosonic interaction and solely depends on the nature of the magnetic field. The density irregularities only provide the wave's momentum. The restoring force is entirely generated by the tension in the magnetic field. Goedbloed and Poedts (2004)[Subsection 5.2.3]

The wave corresponding to $\omega_A^2 = k^2 v_a^2 \cos^2 \theta$ is called the *Alfvén* wave. Notice that its direction corresponds to that of the magnetic field, where $\omega_A = kv_a \cos \theta$ lies in the same direction and $-\omega_A$ in the opposite direction. It should be noted that this solution is non-relativistic. As the magnetic field becomes stronger in comparison to the density, the Alfvén wave becomes a regular electromagnetic wave.

Now, the first roots we had - the magnetosonic waves - are combinations of Alfvén waves and ordinary sound waves. There are two types because the Alfvén and sound waves can either be in phase or in antiphase to one another. In the first case ω_+ the region of high pressure will correspond to a high magnetic field density, which causes the resulting wave to be driven forward by both ordinary hydrodynamic pressure and the tension of the concentrated magnetic field lines. In the other case of ω_- , these same two forces work against each other, slowing the wave.

2.2.4 Magnetohydrodynamic shocks

To derive the Rankine–Hugoniot conditions for MHD shocks, one simply uses eq. (19) as it is already in its Eulerian form and performs the same calculations as for the Rankine–Hugoniot conditions for HD shocks. This yields:

$$\begin{aligned} V_S \Delta \rho &= \mathbf{n} \cdot \Delta(\rho \mathbf{v}) \\ V_S \Delta(\rho \mathbf{v}) &= \mathbf{n} \cdot \Delta(\rho \mathbf{v} \mathbf{v} + (p + \frac{B^2}{2}) \mathbb{I} - \mathbf{B}\mathbf{B}) \\ V_S \Delta E_t &= \mathbf{n} \cdot \Delta((\rho \frac{v^2}{2} + \frac{\gamma}{\gamma-1} p + B^2) \mathbf{v} - \mathbf{v} \cdot \mathbf{B}\mathbf{B}) \\ V_S \Delta \mathbf{B} &= \mathbf{n} \cdot \Delta(\mathbf{v}\mathbf{B} - \mathbf{B}\mathbf{v}) \end{aligned} \tag{31}$$

These equations will not result in an expression for the shock speed which is fundamentally different from the result we found in the HD case. Therefore, we shall now focus on the group speed which is in the MHD case quite peculiar indeed.

2.2.5 Group speed

The wave speed that is derived from the simulations is the group speed and not the phase speed of the waves. We use the relation eq. (9) to calculate this quantity. For the Alfvén waves, this is straightforward and yields:

$$\mathbf{v}_{ga} = \hat{\mathbf{k}} \cos \theta v_a \tag{32}$$

Where θ is again the angle between $\hat{\mathbf{k}}$ and the magnetic field \mathbf{B} .

For the slow and fast magnetosonic waves, this is a lot more involved. A derivation can be found in Liu (2014) [chapter 6]. The result is ($v_{\pm} = \omega_{\pm}/k$):

$$\mathbf{v}_{g\pm} = \frac{v_{\pm}^4(\theta) \hat{\mathbf{k}} - v_s^2 v_a^2 \hat{\mathbf{B}} \cos \theta}{v_{\pm}(\theta) [2v_{\pm}^2 - (v_s^2 + v_a^2)]} \tag{33}$$

Where the hats denote unit vectors. This gives the group speed of the fast and slow magnetosonic modes as a function of the angle θ . In fig. 1 this relation is plotted in polar form for a few different values of the plasma- β . The β used here is one calculated using the dimensionless units introduced in section 2.3. A derivation to get from the value of β to values for v_a and v_s needed to calculate the group velocity can be found in that section as well. We remark that the group speed of the slow-mode along the magnetic field has a maximum speed equal to $\min\{v_a, v_s\}$ and the speed of the fast mode is $\max\{v_a, v_s\}$ along the x -axis.

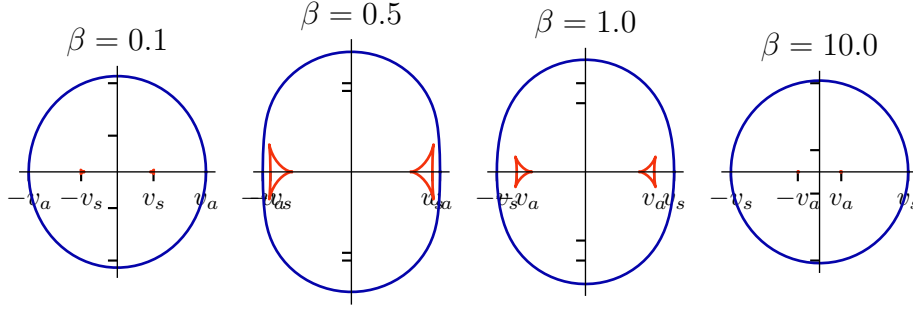


Figure 1: Group speed diagrams for the fast (blue) and slow (red) magnetosonic waves. The magnetic field is oriented along the horizontal axis. The lines represent the group speed of the wave (distance from origin) as a function of the angle θ between the wave vector \mathbf{k} and magnetic field \mathbf{B} .

2.3 Units

The PLUTO code works, in general, with dimensionless code-units. This is done by defining a unit density ρ_0 , unit velocity v_0 and unit length L_0 Mignone and et al. (2018) [Chapter 5]. From these, unit time can be defined as $t_0 = L_0/v_0$. Inspired by eq. (25) and eq. (26) we define $p_0 = \rho_0 v_0^2$ and $B_0 = v_0 \sqrt{4\pi\rho_0}$. Next, we use the substitutions $v_0 \mathbf{v}_u = \mathbf{v}$, $\rho_0 \rho_u = \rho$, $L_0 \mathbf{x}_u = \mathbf{x}$, $t_0 t_u = t$, $p_0 p_u = p$ and $B_0 \mathbf{b}_u = \mathbf{B}$ in eq. (19). Here the subscript u conveys that these numbers or vectors are dimensionless. The units are contained in the factors with subscript 0.

$$\begin{aligned}
 & \frac{\rho_0 v_0^2}{L_0} \rho_u \left(\frac{\partial \mathbf{v}_u}{\partial t_u} + \mathbf{v}_u \cdot \nabla_u \mathbf{v}_u \right) + \frac{\rho_0 v_0^2}{L_0} \nabla_u p_u - \frac{\rho_0 v_0^2}{L_0} \frac{\nabla_u \times \mathbf{B}_u}{\mu_0} \times \mathbf{B}_u = 0 \\
 & \frac{p_0 v_0}{L_0} \frac{\partial p_u}{\partial t_u} + \frac{p_0 v_0}{L_0} \mathbf{v}_u \cdot \nabla_u p_u + \frac{p_0 v_0}{L_0} \gamma p_u \nabla_u \cdot \mathbf{v}_u = 0 \\
 & \frac{B_0 v_0}{L_0} \frac{\partial \mathbf{B}_u}{\partial t_u} - \frac{B_0 v_0}{L_0} \nabla_u \times (\mathbf{v}_u \times \mathbf{B}_u) = 0
 \end{aligned} \tag{34}$$

We see that all the units cancel out and we are left with a set of dimensionless equations. *In the remainder of this report, the subscript u to denote dimensionless quantities will be dropped. When a quantity does have units, these will be explicitly stated.* This highlights an important fact for ideal magnetohydrodynamics: the equations are scale-invariant. For the behaviour of the waves the absolute scales are not important. Only the relative magnitude of the characteristic variables of the wave are relevant. When we have a wave with wavelength λ_1 and frequency f_1 , it will exhibit the same behaviour as a wave with wavelength λ_2 and frequency $f_1 \lambda_1 / \lambda_2$ in the same medium (that is, same Alfvén speed).

Because the ideal MHD equations are in fact dimensionless (without the presence of sources and sinks), we can carry out the simulations in dimensionless units. Later, we can scale our results to match conditions as found in e.g. the solar corona, by choosing appropriate values for ρ_0 , v_0 and L_0 .

The plasma- β in these dimensionless units is defined as

$$\beta = \frac{p}{B^2/2} \tag{35}$$

We find that

$$v_a = \frac{B_0}{\sqrt{\rho_0}} = \sqrt{\frac{2p_0}{\beta\rho_0}} = \sqrt{\frac{2}{\beta}}v_0 \quad (36)$$

and that

$$v_s = \sqrt{\gamma \frac{p_0}{\rho_0}} = \sqrt{\gamma}v_0 \quad (37)$$

These expressions will be necessary to compare the simulation data to the theoretical results from the previous sections.

Notice that the factor 4π is included in the definition of B_0 . This has to be taken into account if we want to calculate magnetic pressure or the plasma- β . The expression for the magnetic pressure/energy density is simply

$$p_m = e_m = \frac{B^2}{2} . \quad (38)$$

This is the reason for the factor 2 instead of 8π in eq. (35) which is commonly found in the literature.

3 Modeling shock waves

As a test case to get acquainted with the PLUTO software we simulated HD and MHD blastwaves in a 2.5D domain. With 2.5D we mean that the grid used in the simulation is 2D, but the vectorfields for the velocity and magnetic field can have non-zero components along the x -axis. The normalization constants for the units used are the following:

$$v_0 = 10^8 \text{ cm/s} \quad L_0 = 10^8 \text{ cm} \quad \rho_0 = 10^9 m_p \text{ cm}^{-3}$$

where m_p is the mass of a proton. These values are of the order of what is commonly found in the solar corona, see Tomczyk, McIntosh, and et. al. (2007). As was noted in section 2.3, the ideal MHD equation are dimensionless. The ideal HD equations are the ideal MHD equations without the terms relating to the magnetic field. Therefore, they are dimensionless as well. In an effort to keep the discussion as general as possible, dimensionless quantities are used in the remainder of the section, unless explicitly stated otherwise. In some cases, empty square brackets $[]$ emphasize that a quantity is dimensionless.

The initial condition for the simulations is a circle with radius 0.3 at higher pressure p_{in} than its surroundings at $p_{out} = 1$. We ran three simulations for different values of p_{in} . The first with a large pressure difference, where $p_{in} = 5$. The other two have a lower pressure difference with $p_{in} = 1.5$ and $p_{in} = 1.05$. We use these different values of p_{in} to highlight the non-linear effects in the shock wave of the case with higher pressure difference.

3.1 Hydrodynamic shock wave

First some technical details of the simulation. The simulation was done on a 1024×1024 grid for a period of $t = 1.5$ and an initial time step of $1e - 4$. The size of the grid is 6 by 6. A snapshot of the variables describing the system was saved every 0.03 time units, for a total of 50 snapshots (excluding the initial condition).

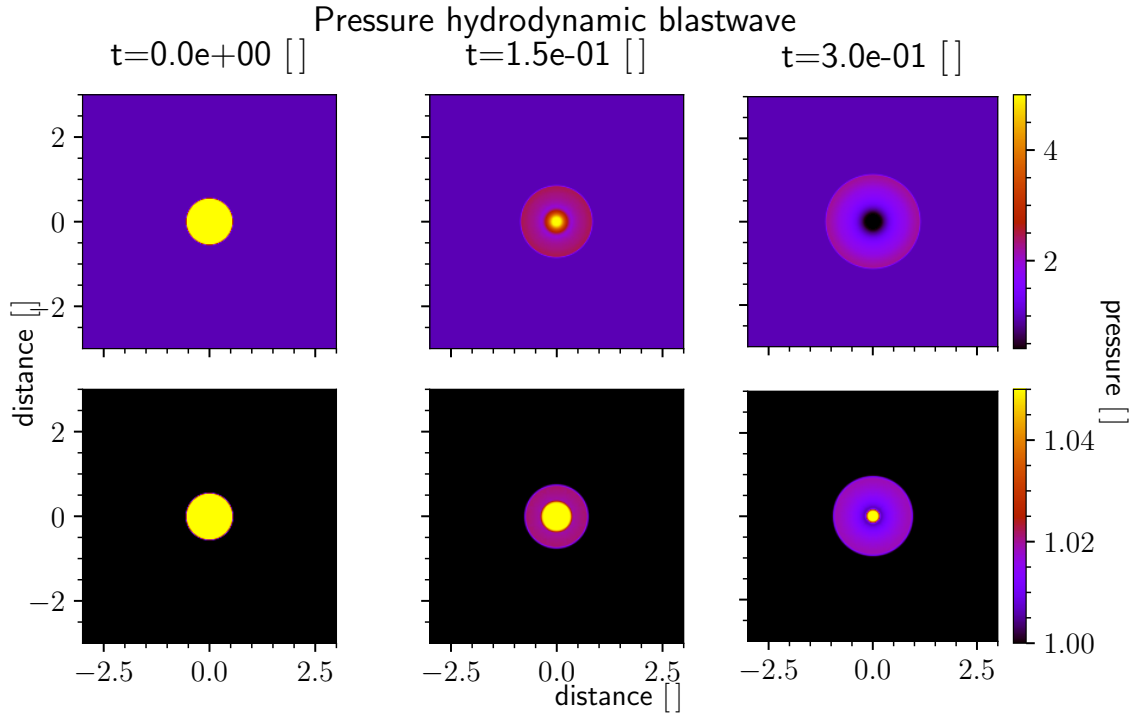


Figure 2: Pressure profile for a blastwave in an ideal fluid at different times. The top row starts with the larger pressure difference of 5/1, the bottom row is the blastwave with the smallest pressure difference of 1.05/1.

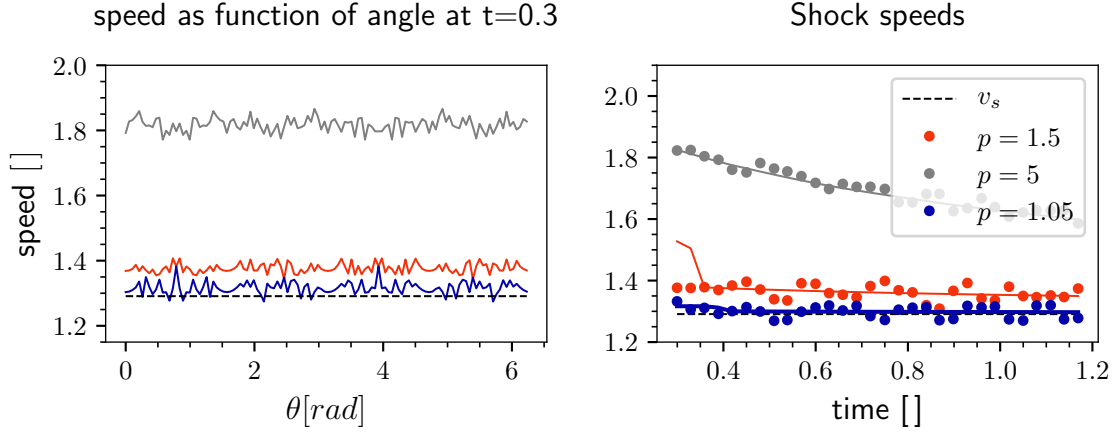


Figure 3: *Left*: Speed at 3 consecutive timestamps averaged together as a function of the angle of propagation for the 3 situations. The averaging was done to lower the noise and find systematic deviations. *Right*: The speed of the wave as a function of time, along the x -axis. The dots represent the speed calculated from the simulation data by deriving the function $x(t)$ that represents the position of the wave front. The lines represent the theoretical shock speed in a Riemann-problem with as high pressure the highest pressure in the domain, and lowest pressure 1. The black dashed line in both graphs is the speed of sound for linear pressure waves in a medium with pressure 1 (code units).

In fig. 2 the pressure profile of both scenarios is plotted for the initial condition and two frames right after the start of the simulation. In fig. 4 the profile is plotted for later times. It is immediately clear that the shock wave with the higher pressure difference travels faster than the other one. However, the general shape of the wave remains the same.

In the right hand plot of fig. 3 the speed of the wave front along the positive x -axis is plotted as a function of time. This confirms that the wave speed is lower with a lower pressure difference. The group speed can be calculated in two ways. The first is to start at a point at the edge of the domain and find the first point on the line from this point to the center with a pressure higher than 1.01 times the background pressure. This way, we get a function $r(t, \theta)$ expressing the distance from the center to the wave front along a line as a function of the angle between this line and the x -axis and time. The speed was calculated using numerical differentiation with the following central difference:

$$f'(t_0) = \frac{f(t + \Delta t) - f(t - \Delta t)}{2\Delta t} + O(\Delta t^2)$$

found in Bultheel (2007). This is the simulated speed, represented by the dots. In the left graph of fig. 3, we see that the speed is isotropic, apart from some deviations. These deviations are mainly due to the discrete nature of the grid, which prevents calculating an exact position of the wave-front. To mitigate this noise, the speeds calculated in all directions were averaged together to get the dots representing the wave speed in the right hand graph of fig. 3.

Using eq. (16) the theoretical speed of a shock in a Riemann problem was calculated, using the highest pressure in the domain as max pressure (p_1) and 1 as the lowest pressure (p_0). This is plotted as the solid lines in fig. 3.

The first 10 snapshots are not included in the right graph of fig. 3. The reason can be seen in fig. 2. When the shock wave starts going outwards, the pressure in the center stays at its original pressure for some more time. We use the max pressure in the domain to estimate p_1 in eq. (16). However for these first frames this is not the maximum pressure in the wave front. It proved to be difficult to accurately detect the maximum of the wave front. Therefore, the first couple of frames were left out. The higher initial speed and sudden drop in fig. 3 for $p = 1.5$ is due to these effects. A closer look to the curve for $p = 1.05$ will reveal something similar.

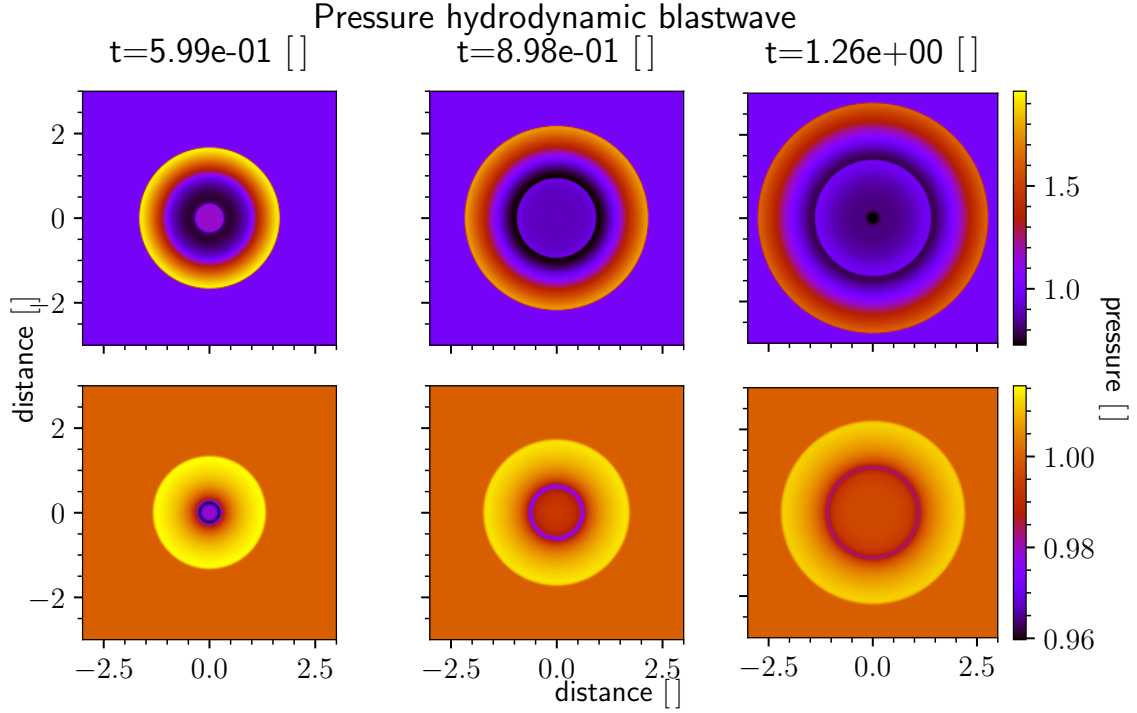


Figure 4: Pressure profile for a blastwave in an ideal fluid at larger timescales. Initial conditions for each row are the same as in fig. 2.

We notice that the curves do match rather closely, proving the ability of the PLUTO code to deal with shocks. The periodic behaviour of dots lying under and above the curve could still be an artefact of the grid discretization. However, no conclusive results were found to prove this. Thus, it could point to a systematic error.

Lastly, in fig. 4, there are new waves appearing from the center. This is due to the nature of a 2.5D simulation. The initial condition has to be interpreted as a long cylinder in 3D, from which a slice perpendicular to this cylinder, is taken for the simulated. The secondary wave fronts can then be seen as waves coming from different points on the cylinder.

We remark that approximating the shock as a Riemann problem is a crude first-order approximation. The PLUTO code calculates flow velocities like this in every integration step Mignone et al. (2007). This small example highlights the importance of robust integrators and Riemann solvers, together with small enough time steps, to accurately model flow variables in the vicinity of large gradients.

3.2 Magnetohydrodynamic shock wave

In the magnetohydrodynamic case the same initial conditions were used as for the hydrodynamic one. A uniform magnetic field in the x -direction was added. To see the effect of the magnetic field, the simulations were carried out for the following values for the plasma- β : $\beta \in \{0.1, 0.5, 1, 10\}$. This is the dimensionless β as given by eq. (35). Figure 5 shows a snapshot of the blast wave at $t = 0.75$ for these different values.

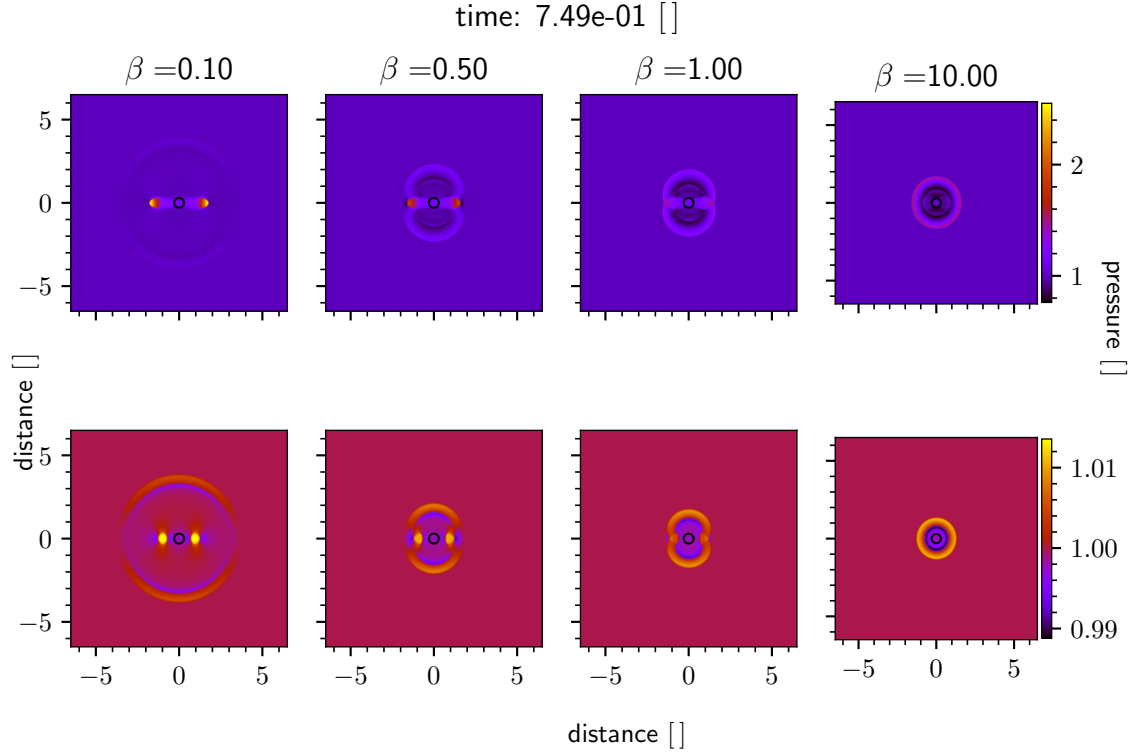


Figure 5: Plots of the pressure of an MHD blastwave with the same initial conditions as in fig. 2: high pressure difference for the top row, lower for the bottom row. The black circle in the middle represents the region of higher pressure in the initial condition.

The simulations for the MHD blastwave used a larger domain: 12 by 12 in code units. This allows us to study the waves at later times when the non-linear effects have diminished because of the lower intensity of the wave. Now we can compare these results to the linear MHD theory from section 2.2.3. The results of the simulation at earlier times can be used to compare the behaviour of an MHD shock to an HD shock.

In the plots with $\beta \in \{0.5, 1\}$ there is a clear distinction between a fast shock wave spreading in all directions, and two smaller waves following the magnetic field. In the plot with $\beta = 0.1$, this fast wave is barely visible closer to the edge of the domain. In contrast, the two small waves stand out from the uniform background. For $\beta = 10$, the fast wave is almost perfectly spherical and clearly visible, whereas the two smaller waves are quite faint. We observe that if the magnetic field is stronger, the fast wave speeds up even further, therefore fading faster because the energy in the wave is spread out more quickly. Meanwhile the energy in the slow mode stays concentrated in a small region. At higher magnetic field strengths the slow mode gets considerably more energetic as well. To go a bit more in-depth, we plotted the diagram depicting the different group speeds to see how well they match. This can be seen in fig. 6 and fig. 7, where the pressure profiles of the waves are plotted at $t = 1.25$. The white dashed lines show the group speed of the fast mode, the grey solid lines the group speed of the slow mode. The black circle is again the region with higher pressure in the initial condition. The group speed diagram was scaled such that the curve for the fast mode would match with the fast wave mode.

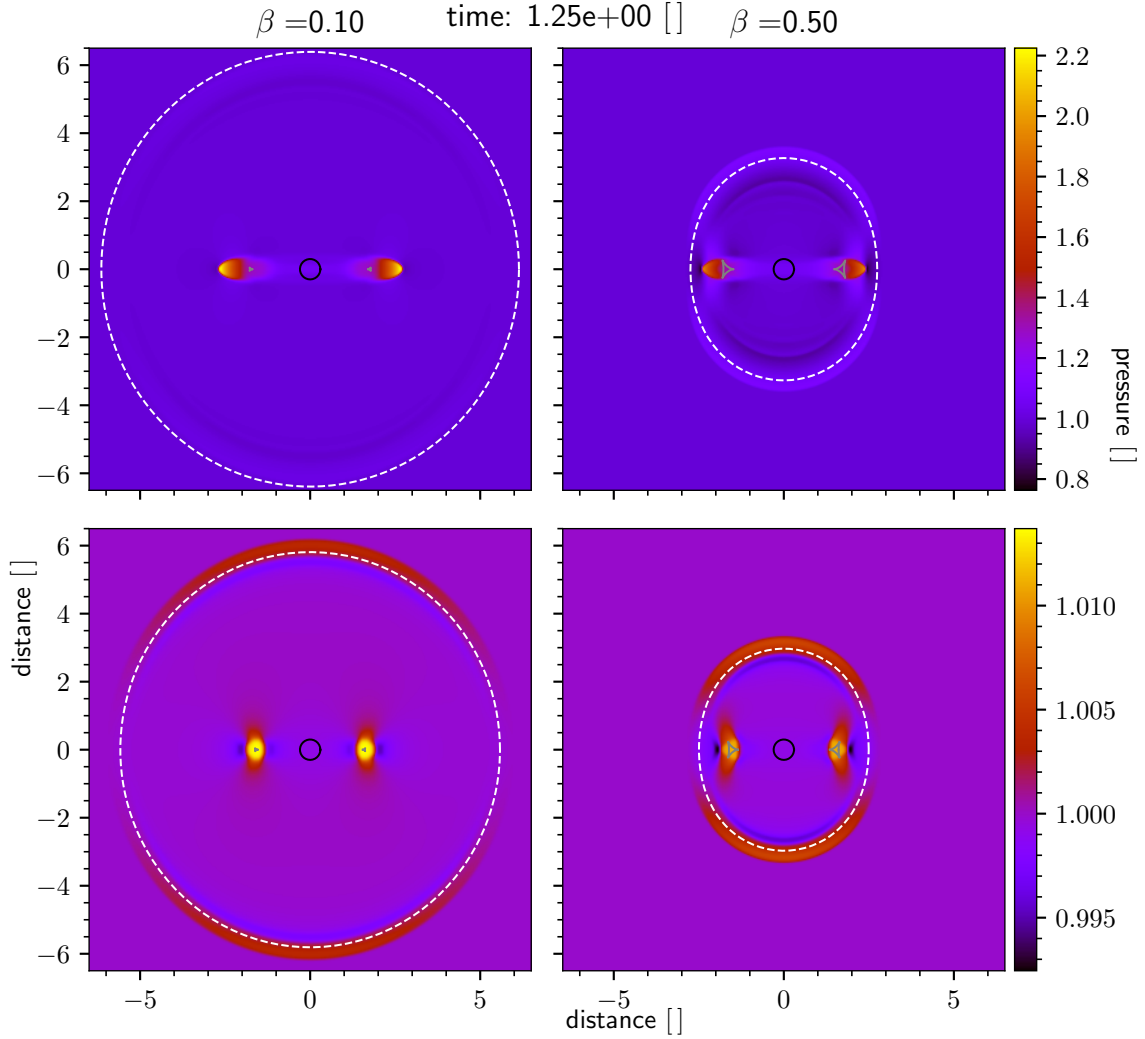


Figure 6: Plots of the pressure wave after 1.25 time units for different values of β . The white dotted line represents the theoretical position of the fast-mode magnetosonic wave. The grey solid lines are the parts of the group speed diagram corresponding to the slow-mode magnetosonic wave. The black circle in the center is the region where the pressure is higher in the initial condition. The top row are plots for simulations where $p_{in} = 5$ at $t = 0$, the bottom row simulations with $p_{in} = 1.05$.

Since the initial condition is not a delta function but a circle with finite radius, we cannot expect a perfect match with the theoretical group speed for linear waves. Instead, a linear wave will be smeared out around the curves for the group speed, as if they were painted with a large brush. Furthermore, when the pressure difference is higher, the non-linear effects will become stronger, leading to deviations from the linear theory.

In figure fig. 6, the two scenarios with a strong magnetic field are shown (low β). The effects of the magnetic field are again very clear, removing the isotropy by deforming the fast magnetosonic wave front, and most strikingly, introducing the slow-mode waves following the magnetic field. Because the slow magnetosonic wave mode only travels along the field lines, its energy remains concentrated. This is the main cause of the large difference in amplitude between the slow- and fast-mode. When the pressure difference is high, the non-linear effects stay important. This causes the slow mode waves in the top row in fig. 6 to travel significantly faster than linear slow wavemode. This can be seen by noting that the yellow or red spots with high pressure are further away from the center than the grey lines denoting the theoretical group speed of the slow wavemode in the top row of fig. 6. In the bottom row, where the pressure difference is a lot smaller, the results match strikingly well to the linear theory.

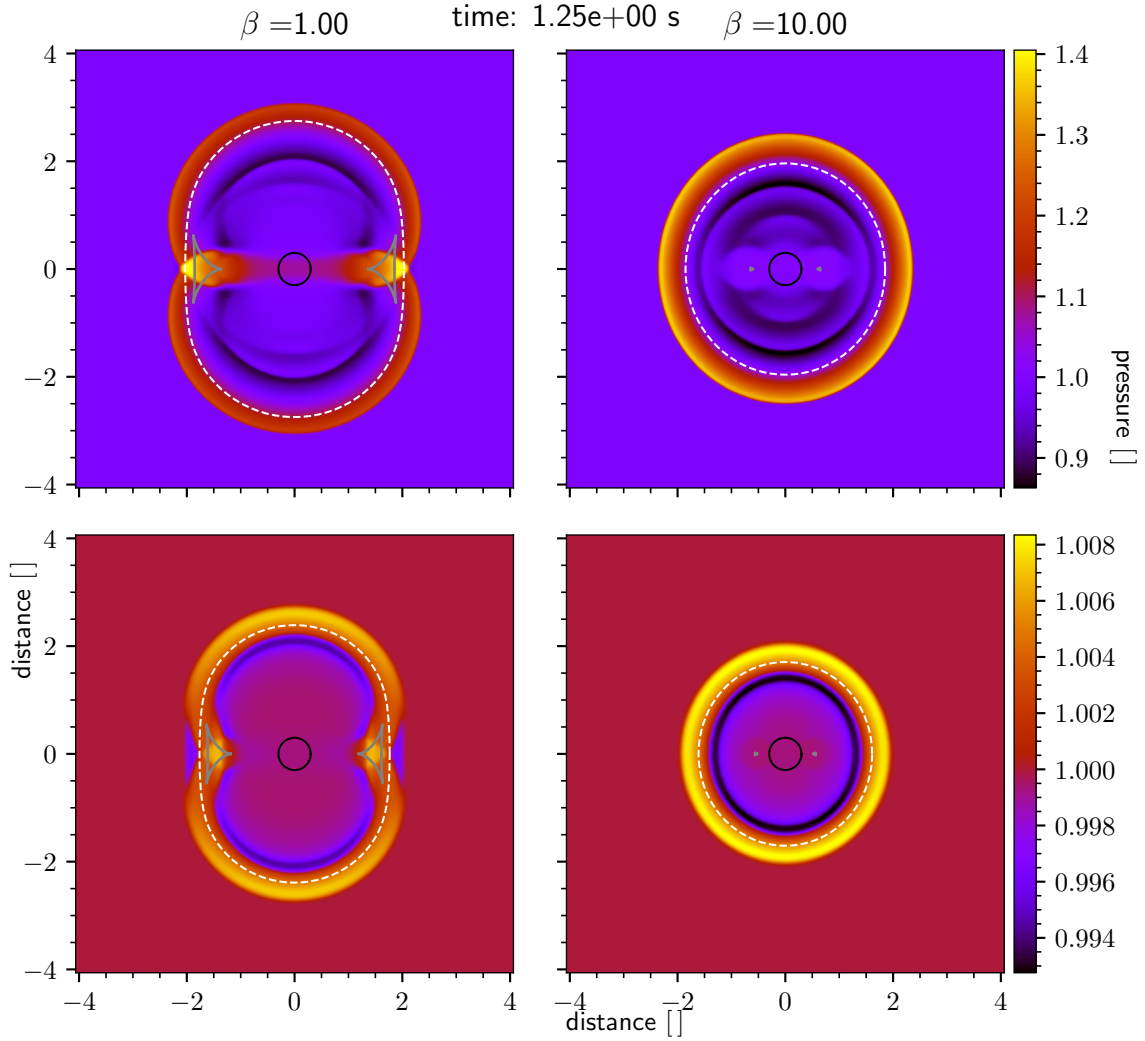


Figure 7: Same as fig. 6 but for different β values.

We also see again that the wave is faster with a higher pressure difference, like with the HD shock waves. Due to the difficulties in accurately detecting the waves in the simulation data, either because they are really faint with small or large β , or because there is a lot of interference between the modes when $\beta \sim 1$, no accurate calculations of the wave speed from the simulation data could be made.

When the magnetic field's strength becomes small, a quick comparison shows that the wave speed goes to the wave speed of an HD-wave, as expected. This can be seen by comparing the rightmost graphs in fig. 7 with the rightmost graphs in fig. 4

4 Coronal hole

In this section we study the interaction of a so-called "coronal hole" with an MHD wave as introduced in the paper Afanasyev and Zhukov (2018) by A.N. Afanasyev and A. N. Zhukov. A coronal hole is a region in the solar corona with much lower density and temperature than the surrounding area. The coronal hole was simulated in 2.5d, assuming that the variables do not depend on z . However, the z -components of vectors do not need to be zero. An ideal equation of state is assumed. This gives the following relation between density, temperature and pressure:

$$nk_B T = p. \quad (39)$$

The total pressure is obtained by adding the magnetic pressure given by eq. (38) to the mechanical pressure, resulting in:

$$p^T = p + \frac{B^2}{2}.$$

From there, the magnitude of the magnetic field is calculated as follows (expressions for code units):

$$B = \sqrt{2(p^T - p)}. \quad (40)$$

The total pressure inside and outside the coronal hole is kept in equilibrium by changing the magnitude of the magnetic field accordingly. In contrast to the magnetic field in the MHD blastwave simulation, the magnetic field is now assumed to lie in the z -direction.

4.1 Initial and boundary conditions

The parameters for the coronal hole are the same as in Afanasyev and Zhukov (2018). The physical size of the domain is a square with side length $2 \times 10^{11} \text{ cm}$, the grid used for the simulation has 1024 by 1024 gridpoints. As a model for the number density and temperature the following was used:

$$\begin{aligned} n(r) &= n_{out} - (n_{out} - n_{in}) \exp(-(r/d)^8) \\ T(r) &= T_{out} - (T_{out} - T_{in}) \exp(-(r/d)^8) \end{aligned} \quad (41)$$

where r represents the distance from the center of the hole and d the characteristic size of the hole. The parameters n_{out} , n_{in} , T_{out} and T_{in} are respectively the plasma number density outside and inside the hole, the temperature outside and the temperature inside the hole. The magnetic field has zero x and y components and the z component is calculated according to eq. (40). The total pressure is calculated by fixing a value B_{out} for the magnitude of the magnetic field far away from the hole and calculated using eq. (40). As a counterpart to the coronal hole model, a coronal plume model was considered as well, again based on Afanasyev and Zhukov (2018). Here the density outside the plume is a lot lower than the density inside. The parameter values for both models can be found in the following table. In fig. 8 and fig. 9 the value of some important quantities at $t = 0$ are shown along a section through the center of the hole or plume respectively.

Parameter	Coronal hole	Coronal plume
n_{out}	$1.0 \times 10^9 \text{ cm}^{-3}$	$1.0 \times 10^8 \text{ cm}^{-3}$
n_{in}	$1.0 \times 10^8 \text{ cm}^{-3}$	$1.0 \times 10^9 \text{ cm}^{-3}$
T_{out}	$1.5 \times 10^6 \text{ K}$	$1.5 \times 10^6 \text{ K}$
T_{in}	$1.0 \times 10^6 \text{ K}$	$1.0 \times 10^6 \text{ K}$
d	$1.5 \times 10^{10} \text{ m}$	$1.0 \times 10^{10} \text{ m}$
B_{out}	4.0 G	3.0 G
v_m	50 km s ⁻¹	125 km s ⁻¹
s_1	20 s	60 s
s_2	16 s	50 s

Table 1: Parameter values taken from Afanasyev and Zhukov (2018). The values used for the initial condition of the coronal hole and coronal plume models.

For the non-linear wave driver, the velocity along x was perturbed at the left boundary. To smoothly pass from 0 to a certain max velocity v_m , stay at this velocity for some time and smoothly return to 0, a combination of two hyperbolic tangents is used in the following formula:

$$v_x(t) = v_m \tanh\left(\frac{t}{s_1}\right) - \frac{v_m}{2} \left(\tanh\left(\frac{t - T_0}{s_2}\right) + 1 \right) \quad (42)$$

The parameters s_1 and s_2 control the steepness of the transition from $v = 0$ to $v = v_m$. T_0 controls the time when the velocity drops back from v_m to 0. At $t = 0$ the velocity starts increasing immediately. This wave propagates with the speed of a fast magnetosonic wave transverse to the magnetic field (since the magnetic field points along the z -direction). Using eq. (33), we find that the group speed of the fast magnetosonic wave transverse to the magnetic field is:

$$v_{g+} = \sqrt{v_a^2 + v_s^2}$$

From fig. 8 and fig. 9, it is clear that this speed is a lot higher outside the plume than outside the hole (about 2.5 times). To obtain a wave of the same physical width in both simulations, we use a shorter wave pulse in the coronal plume model with slightly steeper edges and higher maximum velocity. The parameters for the waves can again be found in tab. 1.

At the right boundary, an open boundary condition is used. For the top and bottom boundaries a periodic boundary condition is used.

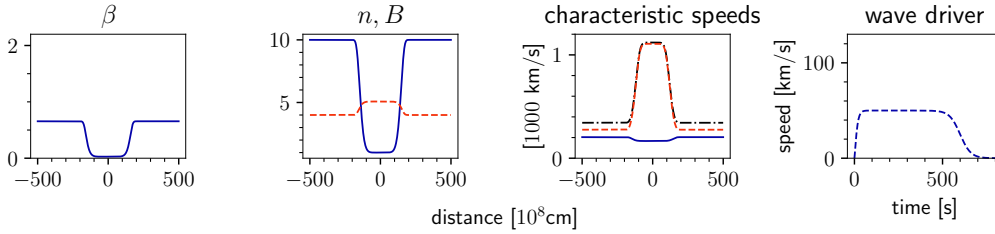


Figure 8: Sections of the initial condition for the *coronal hole* model. *First plot*: plasma beta as given by eq. (35), dimensionless quantity. *Second plot*: the full blue line is the plasma number density in 10^8 cm^{-3} . The red dashed line is the magnetic field in Gauss. *Third plot*: the full line is the sound speed v_s , the dashed red line the Alfvén speed v_a and the dash-dotted black line the fast magnetosonic speed v_+ . *Last plot*: speed profile of the wave driver used. Adapted from Afanasyev and Zhukov (2018)

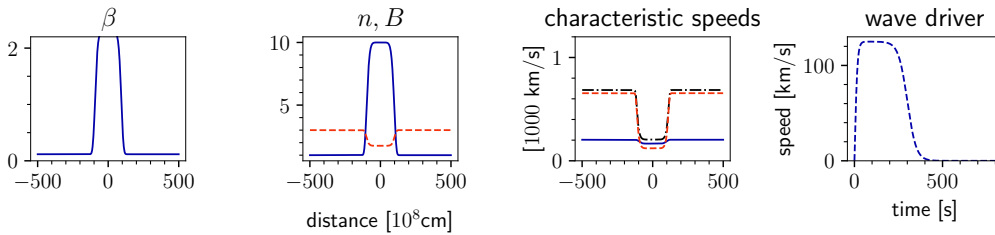


Figure 9: Same as fig. 8 but for the *coronal plume* model.

4.2 Terminology

Before we delve into the discussion of our simulation results, first some comments on the terminology used. Our discussion is mainly based on fig. 11, fig. 12, fig. 10 and fig. 13.

Figure 11 and fig. 12 contain snapshots at 6 different timestamps. For each timestamps, two plots are made next to each other. One plot contains heatmap of the complete simulation domain representing the density. Next to it is again a density heatmap, this time zoomed in on the white box in the plot next to it, providing a better view of the hole/plume. The limits for the colormap are chosen in such a way to highlight the wave fronts, the units of the labels for the colorbar are $10^9 \text{ particles cm}^{-3}$.

When we reference a frame, we talk about the two plots with the same timestamp. If we discuss behaviour inside the hole/plume, this concerns the right plot of the pair. Behaviour outside the structure is about the left plot of the pair.

Figure 10 and fig. 13 contain plots of the density along a cut through the center of the hole or plume along the direction of propagation of the wave. The top and middle plot show the wave outside the structure. The bottom plot zooms in on the wave inside the structure. The dashed lines show the position of the wave front at the bottom edge of the simulation domain.

We will often mention the transmitted and reflected waves, as well as the "main" wave. The transmitted wave is the wave that travels through the structure when it reappears the structure. This is for instance the red ring on the right hand side of the hole in the fourth frame in fig. 11 and the red ring around the plume in the last frame of fig. 12. The reflected wave refers to the wave coming from the left side, top and bottom of the hole/plume right after the main wave has come into contact with the structure. The main wave is the wave generated at the left boundary.

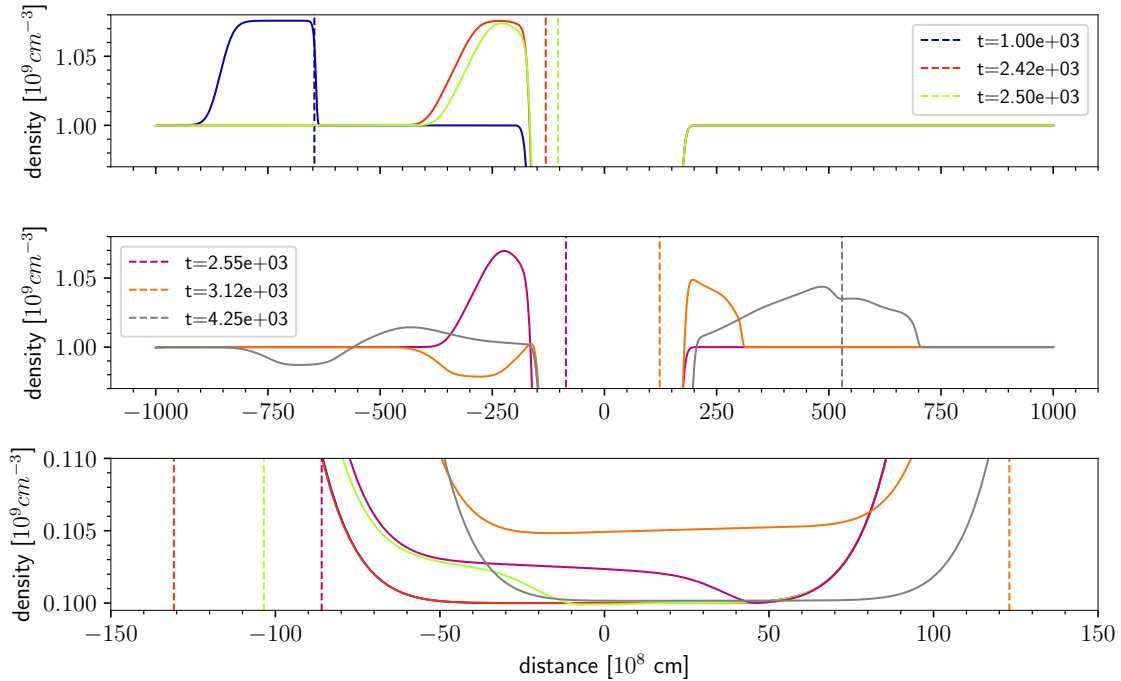


Figure 10: Density profiles along a cut, parallel to the direction of propagation of the wave, through the center of the *coronal hole* at different times. The vertical dashed lines show the position of the wave front at the bottom edge of the simulation domain.

4.3 Results coronal hole

In fig. 11, a couple of density profiles of the *coronal hole* simulation are plotted. From fig. 8 we see that the speed of the wave (the fast magnetosonic speed) is a lot higher inside than outside the hole. Therefore, it is to be expected that the wave transmitted through the hole will be faster than the wave going around. This effect is visible on the heatmaps in fig. 11. In the image at $t = 2.97e + 3s$, the wave front of the transmitted wave is barely visible as the red border to the right of the coronal hole. It is a significant distance ahead of the main wave front. The frames at later times show that the main wave slowly catches up with the transmitted wave. This is probably due to non-linear effects in the shock-wave.

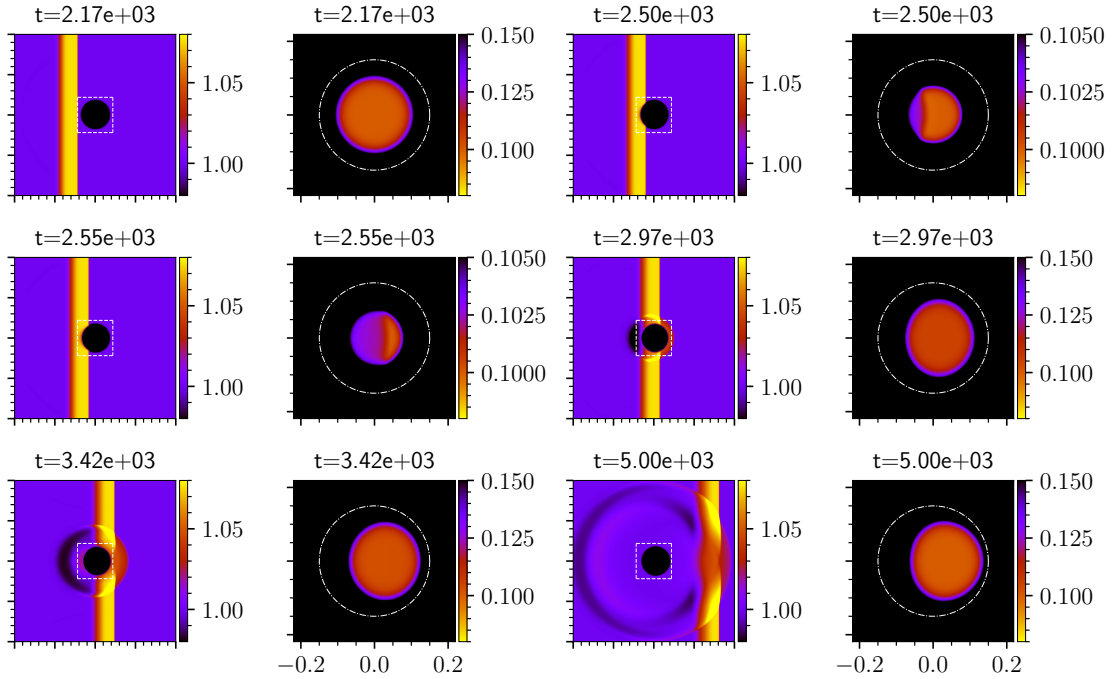


Figure 11: Plots of the density profile of the *coronal hole model* for different times. The plots in the first and third column cover the complete domain of $2e11 \times 2e11$ cm. The plots in the second and last column are zoom in on the plume, the units for the axes are $1e11$ cm. The domain covered is the white box in the plots to the left. The density is measured in 10^9 cm^{-3} . The white circle has the characteristic width d as diameter. In the second and third pair of plots, the density range for the right plot is taken a lot more narrow to highlight the wave transmitted through the coronal hole.

This fast transmission is the most visible in fig. 10. At $t = 2.50e + 3s$, the wave is almost at the center of the hole. Whereas the wave front at the edge of the simulation domain (the green dashed line) is already lagging $100 \times 10^8 \text{ cm}$ behind. Comparing this to the snapshot at $t = 2.55e + 3$, shows that the wave front inside the hole, which has travelled about $50 \times 10^8 \text{ cm}$ since the previous snapshot, propagates about 2.5 times faster than the wave outside the hole, covering only $20 \times 10^8 \text{ cm}$ in the same timespan. We also remark that the effect of the wave on the hole is a sudden increase in density. This is the wave front seen in the snapshots previously discussed. When the wave has passed, the density drops back to its original value. However, the position where it reaches its lowest value is shifted along the direction of propagation of the wave.

Two other phenomena that are readily observed in the last three frames are the diffraction of the main wave around the hole and a rarefaction wave reflected from the hole. At $t = 2.97e + 3$ and $t = 3.42e + 03$, we see the wave bending around the hole and interfering with the transmitted wave. In the last frame, the diffracted wave is visible behind the transmitted wave front, both slightly less energetic than the main wave. The incoming wave also reflects from the hole. In the fourth frame

a black region just behind the hole is visible. This is the reflected rarefaction wave (wave with lower density, in contrast to a shock wave with higher density), closely followed by a wave front with slightly higher density. We see that the reflected wave has opposite phase compared to the incoming wave. Because this wave is almost perfectly circular with the same radius as the transmitted wave, measured from the center of the hole, it is clear that this wave travels at the fast magnetosonic speed as well.

These two effects alter the density of the plasma. The transmitted wave has a lower density compared to the main wave, but higher than the surrounding plasma, whereas the rarefaction wave has a lower density than the surrounding. Therefore, by altering the density they alter the brightness of the plasma. If the hole itself is not directly observable, local dimming of a wave, together with a dimmer wave travelling backwards, may point to a local sudden decrease in density. Furthermore, by carefully studying the form of these waves and amount of dimming, it might be possible to extract more information about the parameters of the non-uniformity such as size and relative change in density.

Lastly, we note that the hole's position is slightly shifted along the direction of propagation of the wave. Apart from a slight deformation of the center of the hole, where the density is almost uniform, its shape remains largely unaltered.

4.4 Results coronal plume

Next we discuss the *coronal plume model*. There is again a reflected wave visible. In fig. 13 we see that now there is a wave front with slightly higher density first, followed by a lower density wake by looking at the snapshots for $t = 1.93e + 3s$ and $t = 2.32e + 3s$. We see that the wave reflected when going from fast to slow magnetosonic speed is in phase, while the reflected wave going from low to high magnetosonic speed is out of phase. This second fact was already observed in the case of the coronal hole, but can also be seen in the zoomed in images of the plume or the density profiles along a cut in the plume. Between the frames at $t = 2.1e + 3s$ and $t = 2.3e + 3s$ in fig. 12 or $t = 1.93e + 3s$ and $t = 2.32e + 3s$ in fig. 13, the wave inside the plume reflects at the boundary and switches from a significantly higher density than the surrounding area to lower density, thus switching phase.

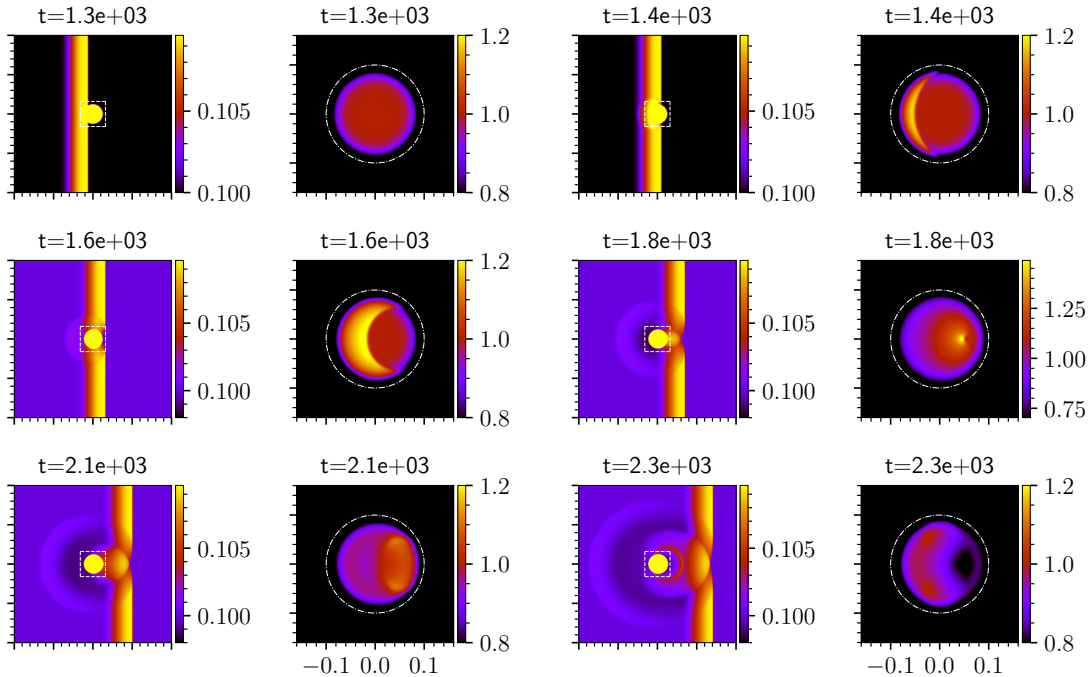


Figure 12: Plots of density profiles for the *coronal plume model*. Same conventions used as in fig. 11

In this case, the transmitted wave is, as expected, slower than the wave outside the hole. This is clearly visible as the line corresponding to $t = 2.32e + 3s$ in the second plot of fig. 13. The original wave front is clearly visible with in its wake a small spike. This is the transmitted wave. Furthermore, the wave gets captured inside the plume, which functions as an echo chamber, emitting secondary wave fronts. Such a secondary wave can be seen as the red ring forming in the last frame in *fig. 12*.

In the plume, the formation of a caustic is observed in the fourth frame of fig. 12. The density increase caused by the wave is concentrated in almost a single point here. This is due to the wave refracting when entering the hole which makes the plume function like a lens. A not perfectly symmetrical shape of the plume will probably lead to less striking caustics. In fact, there were also caustics in the coronal hole model. In the frames at the bottom in figure fig. 11 we see bright edges where the reflected/transmitted wave meets the main wave.

We see again that the structure is moved slightly along the direction of propagation of the wave. If there is a deformation of the coronal plume, it is a lot smaller than in the case of the coronal hole model.

Just as in the coronal hole model the wave is deformed by the interaction with the structure. The transmitted wave forms a secondary wave front behind the main wave front, which is deformed by diffraction around the hole.

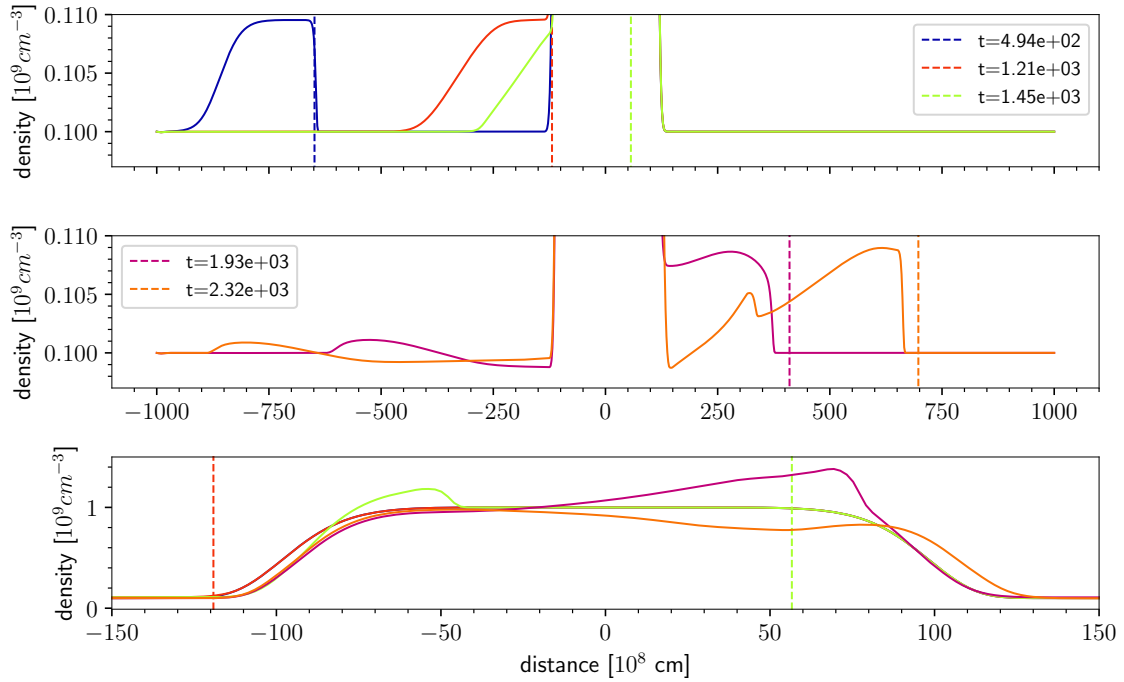


Figure 13: Density profiles along a cut through the center of the *coronal plume* at different times, along the direction of propagation of the waves. The vertical dashed lines show the position of the wave at the bottom edge of the simulation domain.

5 Summary

Firstly, we have given an elementary discussion of HD and MHD theory to serve as a framework for the analysis of the simulation results. The conclusions we have drawn are mainly qualitative. In particular, we have made several essential remarks concerning waves and shockwaves, as a basic understanding in this area is required to understand and interpret the simulations. To be more specific, we have given an explicit expressions for the shock speed (HD) and group velocity (MHD). These are quantitative results which we have used to check the validity and accuracy of the method outlined in this report.

Secondly, we have constructed detailed simulations of both HD and MHD shockwaves and interpreted the output data. The HD case served mainly as a test case. However, we have seen that the speed of the simulated wave for different initial conditions and the shock speed predicted by HD theory line up almost perfectly. Having established the credibility of the method, we repeated the simulations for a nonzero magnetic field strength. As is to be expected, the difference in the results is quite striking. Nevertheless, we have seen once more near-perfect agreement between the theoretical prediction and simulated actuality in the case of small perturbations, both qualitatively and quantitatively.

Finally, we have investigated the influence of a coronal hole on an MHD wave. This problem was certainly more intricate and subtle than the previous one. Therefore we have examined the interaction between the hole and the wave minutely from both ‘perspectives’. That is, we have analysed both the effects on the wave as on the coronal hole itself. Furthermore, we have had a similar setup with a coronal plume simulate a wave-plume collision. This made for an interesting comparison. In both cases the structure was slightly moved in the direction of the wave and both times a clear reflection and diffraction of the wave is visible. However, there is a clear difference in the diffraction of the transmitted wave after the encounter.

6 Final Remarks

The central dogma of present-day physics is that the natural laws must apply everywhere. One could make the case that the theory of magnetohydrodynamics is a perfect example of its success as it seals the chasm between the very largest and smallest scales. Its assumptions are made at the level of elementary particles, discrete charges and molecular degrees of freedom, but its implications reach beyond the scale of stars and even the interstellar medium. Most other theories of physics either lose their validity or applicability at one or both of those extreme scales.

To add to that, it is estimated that most – up to 90 percent Goedbloed and Poedts (2004)– of the matter in the universe (excluding dark matter) is in a plasma-like state. It is therefore safe to say that the applicability of MHD theory is near universal. Both in thermonuclear reactor experiments as in the study of asteroseismology, one must take into account the additional layer of complexity as a consequence of an underlying magnetic field. Furthermore, we have shown the effects of allowing such a magnetic field to dominate the plasma and overshadow the other forces involved.

To end the discussion where we began, the solar corona. A thorough understanding of magnetohydrodynamics and sufficiently precise measurement data may allow us to predict powerful solar seismological activity which can even have damaging effects on our day-to-day lives. Think for example of the 1989 fallout in Quebec due to a solar flare in Earth’s direction. With its extreme conditions and immense dimensions, it is difficult to imagine a more suitable setting for the macroscopic study of plasma. The implications of MHD theory are directly observable via satellite measurements Tomczyk et al. (2007) and even from Earth during a total solar eclipse Goedbloed and Poedts (2004).

Acknowledgements

To close, we would like to extend our exceptional gratitude to our project's counsellor Mijie Shi for his guidance during our time working on this project. We would also like to thank our fellow students Rune Buckinx and Michaël Maex who had the same subject and were kind enough to share some of their research material and have fruitful discussions about the methods to effectively analyse the simulation data.

References

- Afanasyev, A., & Zhukov, A. (2018). Propagation of a global coronal wave and its interaction with large-scale coronal magnetic structures. *Astronomy and Astrophysics*, 614.
- Bultheel, A. (2007). *Inleiding tot de numerieke wiskunde*. Acco.
- Doorselaere, T. V. (2019). *Mathematical introduction to fluid dynamics (course notes)*. Scientia cursdienst.
- Fitzpatrick, R. (n.d.). *Plasma physics*. <https://farside.ph.utexas.edu/teaching/plasma/lectures1/Plasmahtml.html>. (Accessed: 1-04-2020)
- Goedbloed, J. P. H., & Poedts, S. (2004). *Principles of magnetohydrodynamics: with applications to laboratory and astrophysical plasmas*. Cambridge: Cambridge university press.
- Liu, L.-H. (2014). *Elementary space plasma physics second edition*. Airiti Press, Taiwan, R.O.C.
- Mignone, A., Bodo, G., Massaglia, S., Matsakos, T., Tesileanu, O., Zanni, C., & Ferrari, A. (2007). Pluto: a numerical code for computational astrophysics. *The Astrophysical Journal Supplement Series*, 170(1), 228–242.
- Mignone, A., & et al. (2018). *Pluto user's guide*.
- Ogilvie, G. I. (2016). Lecture notes: Astrophysical fluid dynamics.
- Tomczyk, S., McIntosh, S. W., & et. al. (2007, August). Alfvén waves in the solar corona. *Science*, 317, 1192 - 1196.